THE JOURNAL OF PHYSICAL CHEMISTRY C

pubs.acs.org/JPCC Article

# Anisotropic Electron Transport Limits Performance of $Bi_2WO_6$ Photoanodes

Benjamin Moss,* Haonan Le, Sacha Corby, Kazuki Morita, Shababa Selim, Carlos Sotelo-Vazquez, Yunuo Chen, Alexander Borthwick, Anna Wilson, Chris Blackman, James R. Durrant, Aron Walsh, and Andreas Kafizas*

Cite This: J. Phys. Chem. C 2020, 124, 18859−18867 Read Online

ACCESS | Metrics & More | Article Recommendations | Supporting Information

**ABSTRACT:** $Bi_2WO_6$ is one of the simplest members of the versatile Aurivillius oxide family of materials. As an intriguing model system for Aurivillius oxides, $BiVO_4$ exhibits low water oxidation onset potentials (~0.5−0.6 $V_{RHE}$) for driven solar water oxidation. Despite this, $Bi_2WO_6$ also produces low photocurrents in comparison to other metal oxides. Due to a lack of in situ studies, the reasons for such poor performance are not understood. In this study, $Bi_2WO_6$ photoanodes are synthesized by aerosol-assisted chemical vapor deposition. The charge carrier dynamics of $Bi_2WO_6$ are studied in situ under water oxidation conditions, and the rate of both bulk recombination and water oxidation is found to be comparable to other metal oxide photoanodes. However, the rate of electron extraction is at least 10 times slower than the slowest kinetics previously reported in an oxide photoanode. First-principles analysis indicates that the slow electron extraction kinetics are linked to a strong anisotropy in the conduction band. Preferred or epitaxial growth along the conductive axes is a strategy to overcome slow electron transport and low photocurrent densities in layered materials such as $Bi_2WO_6$.

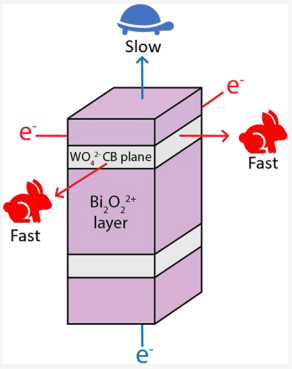


## INTRODUCTION

To mitigate climate change,[1,2] there is a growing need to develop low-cost renewable routes to hydrogen fuel.[3,4] One of the most promising routes to renewable hydrogen is to harness solar energy to convert water into hydrogen and oxygen using photoelectrochemical cells.[5−7] Metal oxides are attractive photoelectrodes as they often show high durability and are typically cheap to produce at scale.[8] To date, the application of oxide-based photoelectrochemical water splitting technologies is limited by a dearth of materials with narrow enough band gaps to effectively harvest the solar spectrum and optoelectronic properties which lend themselves to high efficiencies.[9] The search for efficient, low-cost metal oxides with improved visible light-harvesting characteristics has resulted in an expanding library of ternary and quaternary metal oxides, some of which show promise as photoanodes for the rate-limiting water oxidation half-reaction.[10,11] An unexplored and potentially versatile group of ternary/quaternary oxides is the family of Aurivillius oxides: $(Bi_2O_2)^{2+}(A_{m-1}B_mO_{3m+1})^{2-}$.[2] The layered structure of these materials implies a vast library of possible subphases, each with a distinct set of optoelectronic properties, while studies of B site substitution demonstrate the possibility of band gap engineering to enhance solar harvesting.[12,13] Preliminary studies indicate that some members show promise in photocatalytic and photoelectrochemical applications.[14−16] However, relatively little is known about the factors which govern water oxidation efficiency in even the simplest examples of this diverse and complex family of materials.

$Bi_2WO_6$ is one of the simplest members of the Aurivillius oxide family[17] and possesses a layered structure with alternating $(Bi_2O_2)^{2+}$ and octahedral $(WO_4)^{2-}$ layers, forming an orthorhombic unit cell (Figure 1a).[18] $Bi_2WO_6$ exhibits an ~2.7−2.8 eV band gap,[19] corresponding to a maximum theoretical solar-to-hydrogen efficiency of ~5%.[20] Solar water splitting using $Bi_2WO_6$ was first demonstrated by Kudo et al.[21] It has since been shown that $Bi_2WO_6$ is an *n*-type semiconductor[22] capable of photoelectrochemically oxidizing water.[23−27] $Bi_2WO_6$ photoanodes typically show early onset potentials (~0.5 $V_{RHE}$), but to date, have exhibited low photocurrents.[26,27] Various strategies have been pursued in an effort to improve the photocatalytic activity of $Bi_2WO_6$, which include the use of surface co-catalysts,[26,28] doping,[29−33] and forming heterojunctions.[34−38] However, in order to improve the performance of $Bi_2WO_6$ through rational design, a better understanding of its intrinsic charge carrier behavior is required.[39] To date, there have only been a handful of such studies on $Bi_2WO_6$.[16,40−44] Herein, we carry out the first study of charge carrier dynamics during water oxidation. We determine timescales of bulk recombination, charge separation,

Received: April 21, 2020
Revised: August 5, 2020
Published: August 5, 2020

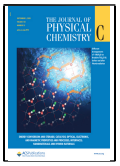







https://dx.doi.org/10.1021/acs.jpcc.0c03539
J. Phys. Chem. C 2020, 124, 18859−18867

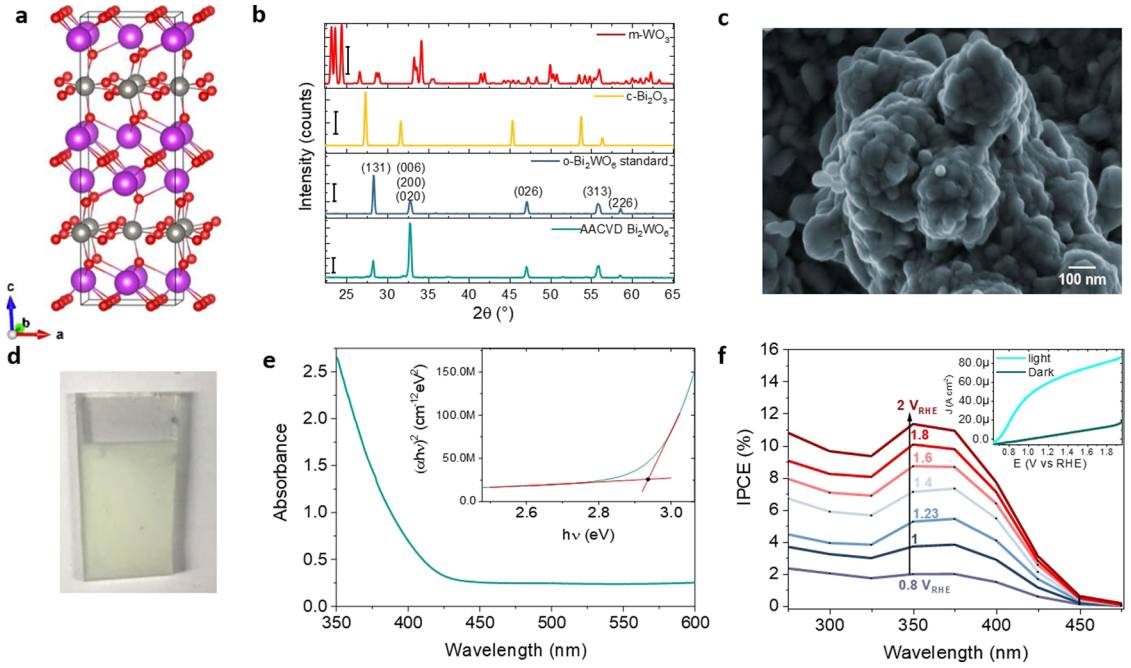


**Figure 1.** (a) Orthorhombic unit cell of $Bi_2WO_6$. Red, purple, and grey spheres correspond to oxygen, bismuth, and tungsten, respectively. XRD patterns of AACVD $Bi_2WO_6$ shown alongside known standards for orthorhombic (o) $Bi_2WO_6$,[54] cubic (c) $Bi_2O_3$,[50] and monoclinic (m) $WO_3$.[51] Scale bar: 300 counts. (c) SEM image of AACVD $Bi_2WO_6$ showing micron-sized mounds composed of smaller crystallites. (d) Photograph of an AACVD $Bi_2WO_6$ film. (e) Absorbance spectrum of AACVD $Bi_2WO_6$ with the inset showing a direct band gap of 2.93 eV. (f) IPCE spectra of AACVD $Bi_2WO_6$ at various applied potentials. Inset: linear sweep voltammograms (10 mV $s^{-1}$) in the dark and under simulated solar irradiation. Electrochemical measurements were performed using front irradiation with phosphate buffer (pH 7) and a three-electrode configuration.

water oxidation, and electron extraction in $Bi_2WO_6$, comparing these to other well-known metal oxides. Electron extraction was found to be 10 times slower than the slowest extraction rate previously reported for an oxide photoanode.[45] Using density functional theory, we link poor electron transport properties to a spatial anisotropy of the conduction band, which is localized in the (001) planes within the material. This leads to new insight into potential design strategies to overcome a poor photocurrent response in $Bi_2WO_6$ and other oxide photoelectrodes exhibiting similar layered crystal structures.

## METHODS

$Bi_2WO_6$ coatings were grown on FTO glass substrates (TEK 15; 2.5 × 2.7 cm) using an aerosol-assisted chemical vapor deposition (AACVD) method, in a cold wall reactor. Substrates were heated from underneath using a graphite heating block. The inlet to the reactor was equipped with a cooling water jacket to prevent any prior decomposition of the precursor before reaching the reactor. The precursor solution contained triphenylbismuth (0.195 g, 22 mM) and tungsten hexacarbonyl (0.0388 g, 5.5 mM) in an acetone: methanol mixture (2:1; 20 mL). The solution was sonicated for 10 min to dissolve the precursors (VWR Ultrasonic Cleaner, 30 W, 45 kHz). The solution was then aerosolized using an ultrasonic humidifier (2 MHz, Liquifog, Johnson Matthey) and carried over the heated FTO substrate (375 °C) using an inert $N_2$ carrier gas (99.99%, BOC) at a flow rate of 300 sccm (MFC, Brooks) over a period of ∼20 min, until the solution had been fully transferred. The coatings formed were subsequently annealed at 550 °C in air for 6 h.

Powder X-ray diffraction (PXRD) was conducted using a Bruker LynxEye X-ray diffractometer equipped with a monochromated Cu-K$\alpha$ (1.5406 Å) X-ray source and compared with standards from the Physical Sciences Data-Science (PSDS) database.[46] Raman spectra were obtained using a Horiba LabRam Infinity equipped a helium−neon laser (633 nm, 25 mW). The system was calibrated with a silicon reference, and samples were analyzed over the 200−1000 $cm^{-1}$ range. Standards were acquired from the RRUFF project database.[47] For scanning electron microscopy (SEM) measurements, a 10 nm chromium film was deposited on samples by sputtering to prevent charging. Images were taken using a LEO Gemini 1525 microscope using a 1.5 keV electron beam. EDX was performed on the same instrument using an Oxford Instruments X-act detector at a beam voltage of 20 keV. High-resolution transmission electron microscopy (HR-TEM) images were obtained using a high-resolution TEM JEOL 2100 with a $LaB_6$ electron source operating at an acceleration voltage of 200 kV. Micrographs were recorded on a Gatan Orius charge-coupled device (CCD). $Bi_2WO_6$ particles were removed from the coatings using a spatula, suspended in *n*-hexane, sonicated, and then drop-cast onto a 400 Cu mesh lacy carbon grid (Agar Scientific Ltd.) for analysis. X-ray photoelectron spectroscopy (XPS) was performed using a Thermo Scientific K-Alpha instrument. The instrument uses monochromated and microfocused Al-K$\alpha$ ($h\nu$ = 1486.6 eV) radiation to eject photoelectrons, which were then analyzed using a 180° double-focusing hemispherical analyzer with a 2D detector. A flood gun was used to minimize sample charging. Spectra were collected at 2 × $10^{-9}$ mbar base pressure. All samples were referenced to the C−C peak of adventitious carbon in the C 1s spectrum at a binding energy of 284.8 eV to correct for any charge that is not neutralized by the flood gun. Data were analyzed using CasaXPS software.[48] Ultraviolet−visible (UV−vis) transmission spectroscopy was performed


https://dx.doi.org/10.1021/acs.jpcc.0c03539
J. Phys. Chem. C 2020, 124, 18859−18867

using a Shimadzu UV−vis 2600 spectrophotometer equipped with an integrating sphere.

All photoelectrochemical analyses were carried out in a homemade PEEK cell with quartz windows. Analyses were typically carried out in 0.1 M phosphate buffer (0.05 M $K_2HPO4$, 0.05 M $KH_2PO_4$; pH = 7) in Milli-Q water (Millipore Corp., 18.2 MΩ·cm at 25 °C), with the exception of our hole scavenger studies, which were carried out in 0.1 M sodium sulphite (pH = 6) and compared with measurements carried out in 0.1 M sodium sulphate (pH = 7). For all measurements, a three-electrode configuration was used, with a Pt mesh counter electrode, an Ag/AgCl reference electrode in sat. $KCl_{(aq)}$ (0.197 $V_{NHE}$ at 25 °C; Metrohm), and a $Bi_2WO_4$ photoanode placed at the working electrode. An Autolab potentiostat (PGSTAT12 with an FRA2 module) was used to apply voltage and measure currents. All applied voltages are reported versus the reversible hydrogen electrode ($V_{RHE}$), converted using the Nernst equation.

$$V_{RHE} = V_{Ag/AgCl} + (0.0591 \times pH) + V^{\phi}_{Ag/AgCl} \quad (1)$$

where $V_{Ag/AgCl}$ is the applied potential versus the reference electrode, and $V^{\phi}_{Ag/AgCl}$ is the standard potential of the reference electrode.

For measuring (photo)current−voltage curves, a 365 nm LED light source was used (LZ1-10 U600, LedEngin Inc.) to photoexcite the photoanode. Light intensity was measured using an optical power meter (PM 100, Thorlabs) coupled with a power sensor (S120UV, Thorlabs). For measuring the incident photon-to-current efficiency (IPCE), an ozone-free xenon lamp (75 W, Hamamatsu) was coupled to a monochromator (OBB-2001, Photon Technology International). The IPCE was calculated using the following equation:

$$IPCE(\%) = (I_{ph} \times 1239.8)/(P_{mono} \times \lambda) \times 100 \quad (2)$$

where $I_{ph}$ is the photocurrent ($mA{\cdot}cm^{-2}$), 1239.8 is the multiplication factor of Planck's constant with the speed of light (eV.nm), $P_{mono}$ is the light power at a given wavelength ($mW{\cdot}cm^{-2}$), and $\lambda$ is the wavelength of the monochromated light (nm).

Ultrafast transient absorption spectroscopy (uf-TAS), from the femtosecond to nanosecond timescale, was measured in transmission mode using a regeneratively amplified Ti:sapphire laser system (Solstice, Spectra-Physics) and Helios spectrometers (Ultrafast Systems), which generates 800 nm laser pulses (92 fs pulse width, 1 kHz repetition rate). To generate the pump, a fraction of the 800 nm beam was directed through a sequence of optical parametric amplifiers (TOPAS Prime, Spectra-Physics) and a frequency mixer (NIR/UV−vis, Light Conversion) to tune the excitation wavelength to 355 nm. The intensity of the pump was modulated using neutral density filters and measured using an energy meter (VEGA, P/N 7Z01560, OPHIR Photonics), fitted with a 0.5 mm diameter aperture. The pump beam at the sample was ≥0.5 mm. A visible white light continuum (WLC) was used as the probe, generated from a fraction of the 800 nm pulse, focused onto a Ti:sapphire crystal. The probe beam was delayed with respect to the pump beam using a motorized delay stage to alter the path length of the probe beam before generation of the WLC. To reduce the noise, the WLC was split into two beams, one of which is passed through the sample and the other used as a reference. Both beams were subsequently focused onto separate fiber-optic coupled, multichannel spectrometers (CMOS sensors). Alternate pump pulses were blocked using a synchronized chopper (500 Hz). As such, absorption spectra of the excited and unexcited sample were obtained to determine the time-resolved absorption difference spectrum. Time zero was then adjusted to match the rise of the signal at each wavelength. The presented decay kinetics were averaged over a spectral range of ca. 10 nm. Measurements were carried out in air.

Slower timescale transient absorption spectroscopy, from the microsecond to second timescale, was measured in the transmission mode. A Nd:YAG laser (OPOTEK Opolette 355 II, ∼6 ns pulse width) was used as the excitation source, generating 355 nm UV light from the third harmonic (∼1.5 $mJ{\cdot}cm^{-2}$ per pulse, repetition rate of 0.65 Hz). The probe light was a 100 W Bentham IL1 quartz halogen lamp. Longpass filters (Comar Instruments) were placed between the lamp and the sample to minimize short-wavelength irradiation of the sample. Transient changes in absorption/diffuse reflectance from the sample were collected using a 2″ diameter, 2″ focal length lens and relayed to a monochromator (Oriel Cornerstone 130) and measured at select wavelengths between 500 and 1100 nm. Time-resolved changes in light transmission were collected using a Si photodiode (Hamamatsu S3071). Data faster than 3.6 ms were recorded using an oscilloscope (Tektronix DPO3012) after passing through an amplifier box (Costronics), whereas data slower than 3.6 ms were recorded using a National Instruments DAQ card (NI USB-6251). Each kinetic trace was obtained from the average of between 100 and 250 laser pulses. Acquisitions were triggered by a photodiode (Thorlabs DET10A) exposed to laser scatter. Data were acquired and processed using home-built software written in LabVIEW. Measurements were carried out in situ in 0.1 M phosphate buffer with our homemade PEEK cell in a three-electrode configuration. The voltage was applied using an Autolab potentiostat (PGSTAT 101, Metrohm). Transient photocurrents (TPC) were measured simultaneously using an oscilloscope.

Plane-wave density functional theory (DFT) calculations were performed using VASP,[49−51] and the atomic structures were visualized using the VESTA package.[52] Geometry optimization[49] was performed with the PBEsol exchange−correlation functional on a primitive cell consisting of 36 atoms, while the density of states and the band structures were calculated with the HSE06 exchange−correlation functional. A *k*-point sampling of 5 × 5 × 2, a plane-wave cutoff of 550 eV, and convergence criteria of $10^{-8}$ eV were employed. The optimized crystal structure has been uploaded to an open repository at https://github.com/WMD-group/Crystal_structures.

## RESULTS AND DISCUSSION

$Bi_2WO_6$ films were grown on FTO glass substrates using an aerosol-assisted chemical vapor deposition (AACVD) method and a previously reported setup (see the Methods section for details).[53] X-ray diffraction (XRD) pattern of the resulting film is shown in Figure 1b. Phase-pure orthorhombic $Bi_2WO_6$ ($P2_1ab$; $a$ = 5.4559 Å, $b$ = 5.4360 Å, $c$ = 16.4297 Å, $\alpha = \beta = \gamma = 90°$)[54] is observed with preferred growth of the (006), (200), and (020) planes. Scherrer line broadening analysis[55] showed that the average crystallite diameter of the $Bi_2WO_6$ coating was ∼50 nm. A LeBail refinement of our XRD data against a crystallographic standard (Figure S0a) indicates that differences in between the measured pattern and the standard



https://dx.doi.org/10.1021/acs.jpcc.0c03539
J. Phys. Chem. C 2020, 124, 18859−18867

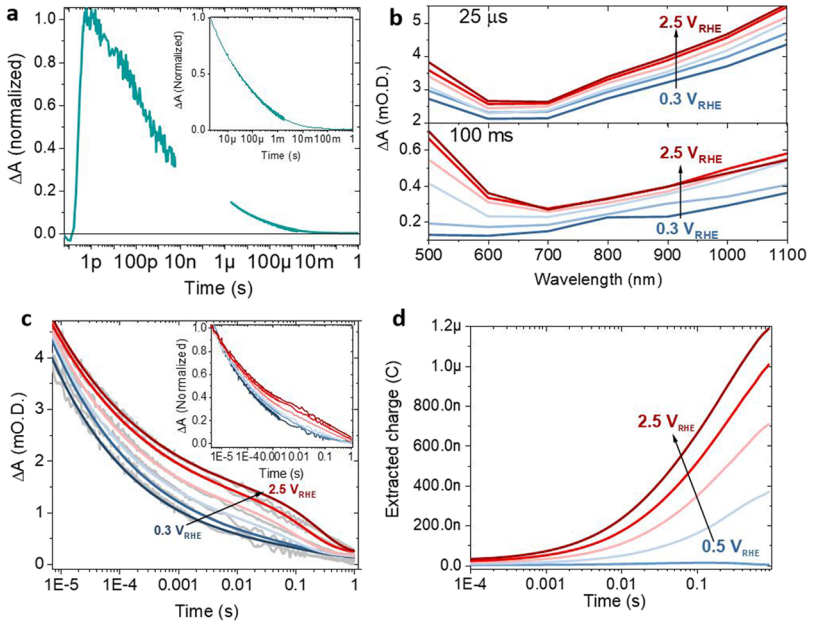


**Figure 2.** (a) Normalized transient recombination kinetics from the ps−s timescale, measured at 650 nm under an inert atmosphere. The inset shows normalized recombination kinetics from $\mu$s to s. (b) Transient spectra of AACVD $Bi_2WO_6$ at 25 $\mu$s and 250 ms at 0.3, 0.5, 1, 1.5, 2, and 2.5 $V_{RHE}$. (c) Transient kinetics measured at 500 nm at 0.3, 0.5, 1, 1.5, 2, and 2.5 $V_{RHE}$. Experimental data are shown in gray, and the results of fitting of the sum of a power law function plus an exponential function are shown in color. Inset: TA kinetics normalized at 5 $\mu$s. (d) Time-resolved charge extraction measured during TA experiments, showing 50% charge extraction times of ∼100 ms. Conditions for b−d: front irradiation using phosphate buffer (pH 7) and a three-electrode configuration.

can be attributed to the preferred growth. This is consistent with a more detailed comparison of the measured pattern against the standards for $WO_3$ and $Bi_2O_3$ (Figure S0b), where the absence of peaks at 24.4° and 45.35° (Figure S0c,d) indicates that any impurity phases are found in concentrations beneath the detection limit of the diffractometer. Purity is further corroborated by XPS (Figure S1), which indicates that the film is primarily composed of $W^{6+}$, $Bi^{3+}$, and $O^{2-}$ states with a Bi: W: O ratio of 2.0: 0.74: 5.3, which is close to the expected stoichiometric ratio (see Figure S1 for a detailed discussion of oxidation states).

High-resolution scanning electron microscopy (SEM) images of the AACVD $Bi_2WO_6$ films are shown in Figure 1c. The coatings are composed of rough, micron-sized mounds, themselves composed of smaller (< 100 nm diameter) particles. A cross-sectional SEM (Figure S2) image reveals the films to be, on average, ∼1.5 $\mu$m thick, with good film coverage and few pinholes. EDX analysis (Figure S3) indicates that the $Bi_2WO_6$ coatings contained Bi, W, and O. However, some nanoscale regions of high W content and low Bi content were observed (Figure S3). These are attributed to $WO_3$ impurity crystal growth at concentrations below the resolution of XRD (roughly ≤1%). Due to the low concentration of $WO_3$ and the distinct behavior of the $Bi_2WO_6$ films studied herein from the AACVD $WO_3$ films made previously by our group,[45] we do not consider this minor impurity to be a significant factor influencing the behavior of the films. High-magnification SEM images (Figure S4) reveal that the micron-sized mounds of the coating are themselves composed of interconnected nanoparticles ranging in diameter from ∼20−100 nm, consistent with the results of Scherrer analysis.

The optical characteristics of the AACVD $Bi_2WO_6$ films are evaluated as shown in Figure 1d,e, which, respectively, show a photograph of a typical film and the corresponding optical absorbance spectrum. Films were opaque with a slight yellow color. This is reflected in the absorbance spectrum, which shows an absorbance onset around 425 nm superimposed on a flat background of 0.25 a.u. induced by strong scattering (Figure S5). Consistent with the absorbance onset, a direct allowed band gap of 2.93 eV was measured using the Tauc method, similar to previous literature findings.[25,37]

We assessed the performance of AACVD $Bi_2WO_6$ as photoanodes for the photoelectrochemical oxidation of water. IPCE spectra at various applied potentials are shown in Figure 1f. A maximum IPCE of 4% was observed with 375 nm light at 1.23 $V_{RHE}$, with a roughly linear dependence of efficiency on the applied potential. A distinct wavelength dependence is also observed, with IPCE increasing with decreasing wavelength until 350−375 nm, presumably due to increased photon absorption, after which a decrease is observed. A typical current−voltage curve is shown in the inset of Figure 1f. Here, the onset of photoelectrochemical water oxidation is observed at 0.6 $V_{RHE}$ with a photocurrent at 1.23 $V_{RHE}$ of ∼0.06 mA $cm^{-2}$. The photoelectrochemical stability of our $Bi_2WO_6$ photoanodes was measured at 1.23 $V_{RHE}$ under chopped, intense 375 nm irradiation (Figure S6). Within a few minutes, the photocurrent dropped from ∼3.2 to ∼2.8 mA $cm^{-2}$. However, after this initial drop (equivalent to an ∼19% loss in performance), the photocurrent remained approximately constant for the 15 h testing period (see Figure S6 for further discussion).

The performance of the AACVD $Bi_2WO_6$ coatings studied herein agrees well with the literature trend of relatively early onset potentials but poor photocurrent density (see Table S1 for a comparison). To further understand the origin of low photocurrent densities relative to other similar materials, we turned to transient absorption spectroscopy (TAS) combined with simultaneous transient charge extraction measurements,


https://dx.doi.org/10.1021/acs.jpcc.0c03539
J. Phys. Chem. C 2020, 124, 18859−18867

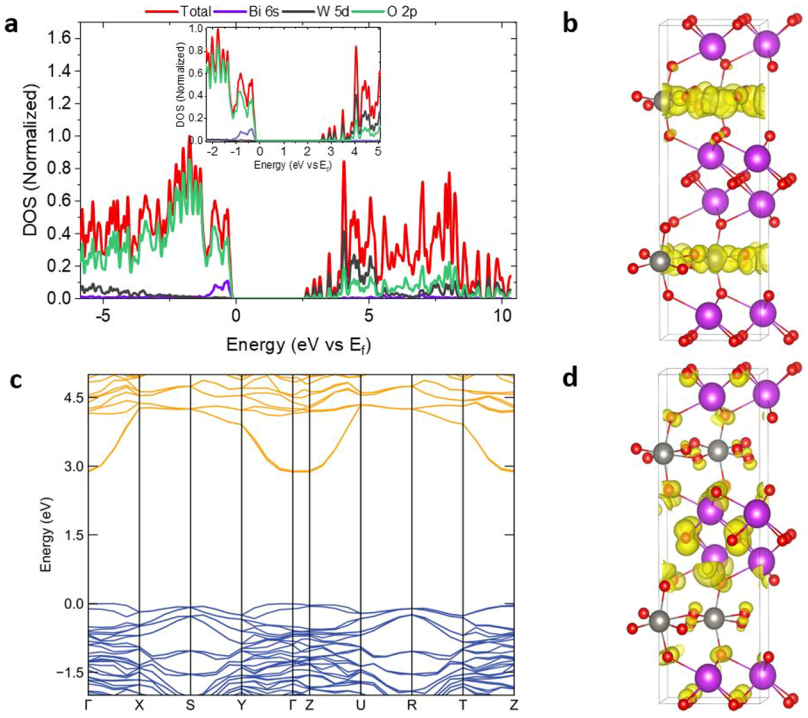


**Figure 3.** (a) Normalized total and partial density of states of $Bi_2WO_6$ (DFT-HSE06) with the inset showing the region around the valence band maximum and conduction band minimum. (b) 0.003 e/Å$^3$ isosurface for the conduction band of $Bi_2WO_6$. (c) Band structure for $Bi_2WO_6$ showing strong in-plane conduction band dispersion between Γ and X or Γ and Y but weak out-of-plane dispersion between Γ and Z. (d) 0.003 e/Å$^3$ isosurface for the valence band of $Bi_2WO_6$.

comparing these results to other metal oxides known to exhibit higher photocurrents such as $TiO_2$, $WO_3$, and $BiVO_4$.

To better understand the influence of recombination on the photocurrent produced by $Bi_2WO_6$, we performed ultrafast (fs−ns) and slow (μs−s) TAS under an inert atmosphere. Here, charges are not separated by a depletion layer and can only recombine. The rates of recombination in the absence of a space charge layer (hereafter, "bulk" recombination) can vary by orders of magnitude between different metal oxides on ultrafast timescales, which in turn can impact efficiency. For example, the $t_{50\%}$ of transient photogenerated charge in $Fe_2O_3$ under an inert atmosphere ranges from 10−30 ps, while transients for $TiO_2$ measured under the same conditions have a $t_{50\%}$ of 1000−2000 ps.[56] Figure 2a shows the bulk TA recombination kinetics of $Bi_2WO_6$ from fs to s. Electron−hole recombination was investigated by probing at 650 nm following excitation with a 355 nm laser flash. A relatively slow decaying transient was observed, with a $t_{50\%}$ decay of ∼0.20 ns from 2 ps being observed, which decays more slowly at lower excitation densities, indicative of bimolecular-type recombination (i.e., a nongeminate electron/hole recombination, see Figure S7 for intensity dependence).[57] This is faster than anatase $TiO_2$ on ultrafast timescales[56,58] but slower than $Fe_2O_3$, $BiVO_4$, or $WO_3$.[56,59] On slower timescales, power law ($\Delta OD \propto t^{-\alpha}$ where $\alpha \approx 0.26$) recombination dynamics were observed. Power law decays occur in a broad range of metal oxides, arising when ideal "bimolecular" electron/hole recombination ($\alpha = 1$) is disrupted by a multiple trapping process in which a carrier must be repeatedly thermally excited in order to move and ultimately recombine.[57,60] Here, a $t_{50\%}$ value of around 100 μs is observed from 1 μs, commensurate with slow timescale bulk recombination in $WO_3$ (10−100 μs, see Table S2 and Figure S8 for comparison to literature studies).

To interrogate the role of recombination in the presence of a charge-separating depletion layer[61,62] in limiting the photocurrent, the TA kinetics of the AACVD $Bi_2WO_6$ photoanodes were monitored in situ under water oxidation conditions. Figure 2b shows the TA spectrum at 25 μs (upper panel) and 250 ms (lower panel) after front irradiation with a 1.2 mJ cm$^{-2}$ laser pulse at various applied potentials (0.3 to 2.5 $V_{RHE}$). A strong increase in amplitude at 250 ms is shown in blue ($\lambda_{max}$ ∼ 500 nm) relative to longer wavelengths as the potential is increased. This effect has previously been observed in $TiO_2$,[63] $BiVO_4$,[61] and $Fe_2O_3$[56] photoanodes and is attributed to improved charge separation arising from the growth of a depletion layer with increasing potential. As such, we attribute the increased signal observed at ∼500 nm to persistent, surface-separated holes at the $Bi_2WO_6$ surface. This effect is clearly visible in the transient kinetics at 500 nm (Figure 2c). Here, a component exhibiting power law decay kinetics is observed at low applied potentials (0.3 and 0.5 $V_{RHE}$). As the $t_{50\%}$ of this decay is around 100 μs—similar to that observed under an inert atmosphere (Figure 2a)—we assign this decay component to bulk recombination occurring outside the space charge layer. As the potential is increased, a second, more persistent component in the TA emerges at later times (attributed to the separation of charge in the depletion layer), which then decays exponentially. Fitting these decays with the sum of a power law and an exponential decay function reveals that persistent, exponentially decaying holes at potentials ≥1 $V_{RHE}$ decay with an approximate rate constant of approximately 7 s$^{-1}$ (see Figure S9 for details/fitting parameters). For potentials exceeding 1 $V_{RHE}$, the transient charge extracted during the experiment (Figure 2d) does not decrease at later


https://dx.doi.org/10.1021/acs.jpcc.0c03539
J. Phys. Chem. C 2020, 124, 18859−18867

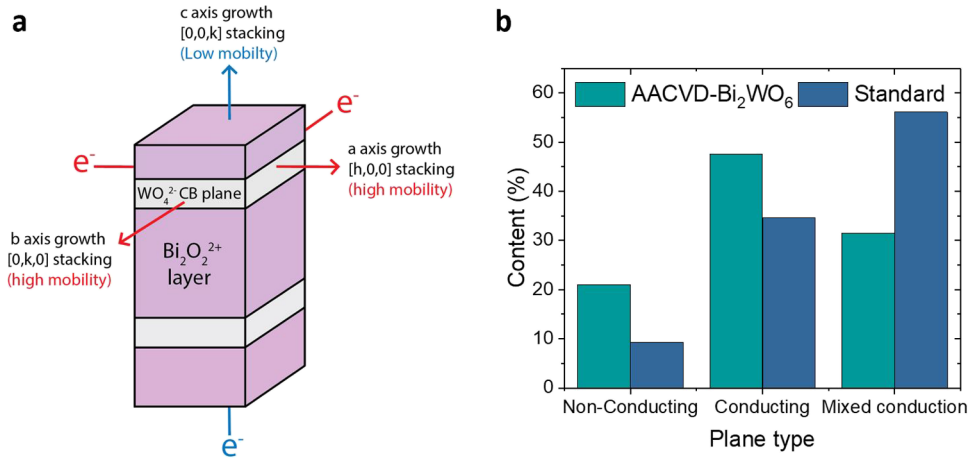


**Figure 4.** (a) Schematic of the layered orthorhombic unit cell of $Bi_2WO_6$ illustrating the connection between electron transport and preferred growth arising from a CB limited to planes in the material. (b) Quantification of the growth planes of the material, in comparison to a single crystal standard categorized according to the directions of growth shown in (a). Mixed mobility planes are planes which grow in the crystal in both favorable and unfavorable directions simultaneously.

times. A decrease would indicate the back recombination of separated surface holes with bulk electrons, rather than a reaction.[61,62] As this is not present, we assign this time constant to the reaction of holes with water.[61,62] The observed rate constant of ca. 7 $s^{-1}$ matches with that observed in $TiO_2$ (2−5 $s^{-1}$),[63] faster than $Fe_2O_3$ (0.7 $s^{-1}$)[64] and $BiVO_4$ (1.3 $s^{-1}$),[61] but significantly slower than $WO_3$ (~2000 $s^{-1}$).[45] As with other metal oxides,[61] the amplitude of this long-lived exponential decay phase correlates with the photocurrent, providing further indication that this decay arises from the reaction of photogenerated holes with water (Figure S10).

Transient electron extraction kinetics, measured simultaneously during TA experiments, are shown in Figure 2d. Remarkably, slow extraction kinetics are observed, differing by orders of magnitude from other metal oxides studied using the same technique. For example, even at the strongest potential studied herein, 50% electron extraction times are around 100 ms. This is at least 10 times slower than the slowest extraction times previously observed in a metal oxide ($WO_3$ ~ 10 ms).[45] Furthermore, in $WO_3$, the photogenerated electrons travelled twice as far (ca. 3.6 $\mu$m thick film) to reach the external circuit than the AACVD $Bi_2WO_6$ films studied herein (ca. 1.5 $\mu$m thick film), yet did so 10 times faster. Other oxides, such as $Fe_2O_3$ and $BiVO_4$, show 50% extraction times around two orders of magnitude faster compared to AACVD $Bi_2WO_6$ (ca. 1 ms).[20,59]

To understand the origin of the remarkably slow electron extraction, we turned to density functional theory (DFT) using the HSE06 functional to precisely calculate the band structure (see the Methods section for details). Figure 3a shows the normalized total and partial density of states for $Bi_2WO_6$. The valence band (VB) maximum projects onto both Bi 6s and O 2p states. This coupling of Bi 6s and O 2p orbitals leads to an upward dispersion of the VB and a narrower band gap than would otherwise be expected.[65] Consistent with the results of a previous theoretical study screening Aurivillius oxides,[13] the conduction band (CB) minimum projects predominantly on W 5d states with some O 2p density. The CB exhibits a strong spatial anisotropy, illustrated by the isosurface shown in Figure 3b. Here, the CB is confined to the $(WO_4^{2-})_n$ planes. The impact on the band structure is evident (Figure 3c) as strong CB dispersion is observed along the <100> (Γ to X) and <010> (Γ to Y) directions. In contrast, negligible dispersion is observed along the <001> ( Γ to Z) direction, corresponding to the out-of-plane interaction between the $WO_4^{2-}$ units. Anisotropy in the band dispersion (effective masses) is compounded by the fact that on the ms−s timescale, electron transport occurs through thermally activated polaron hopping.[45] Here, the probability of hopping (tunneling) decays exponentially with distance, meaning that hopping from one ($WO_4^{2-}$) subunit to another across a larger $(Bi_2O_2^{2+})_n$ plane will be slower than hopping between ($WO_4^{2-}$) subunits within the plane. This is consistent with the observation that electron extraction is 10 times slower in $Bi_2WO_6$ than in $WO_3$, where the connectivity is more isotropic. The same anisotropic conduction does not occur for holes, as the O 2p-based valence band is not confined to a given plane (Figure 3c).

To understand the impact of anisotropic electron transport in the AACVD $Bi_2WO_6$ films studied herein, we return to our XRD data (Figure 1b). From simple inspection of the data, it is apparent that growing $Bi_2WO_6$ by AACVD leads to preferred growth in the randomly oriented crystallites that make up the micron-sized mounds in the film. By performing a LeBail refinement of our XRD data (Figure 1b) against a crystallographic standard (o-$Bi_2WO_6$ shown in Figure 1b), the relative concentrations of different planes in AACVD $Bi_2WO_6$ can be quantified and compared to the crystallographic standard (Figure S11).

This analysis reveals that Miller planes in the (131) direction ($2\theta$ = 28.3°) grow less, whereas the Miller planes in the (006), (200), and (020) directions ($2\theta$ = 32.603, 32.809, and 32.925°, respectively) are enhanced. Figure 4a shows a simplified schematic of the orthorhombic unit cell of $Bi_2WO_6$ and illustrates the connection between different modes of preferred growth and electron transport. Hypothetically, very strong preferred growth of the (h,0,0) or (0,k,0) planes would result in nanorods with conduction band planes growing along the length of the rod. Strong preferred (h,k,0) growth would lead to sheets with similar favorable conduction. However, stacking of the (0,0,l) planes would lead to growth orthogonal to the favorable directions of electron transport. Figure 4b shows the result of categorization of growth planes into three categories: growth planes along which CB electrons would exhibit mobility in the presence of an electric field and are thus


https://dx.doi.org/10.1021/acs.jpcc.0c03539
J. Phys. Chem. C 2020, 124, 18859−18867

more conductive (i.e., (h,0,0), (0,k,0), or (h,k,0)); low mobility, poorly conducting (0,0,l) growth planes, and planes in which growth in favorable and unfavorable directions would occur simultaneously ("mixed mobility," (0,k,l), (h,0,l), and (h,k,l) planes). From this analysis, it is apparent that the crystallites that make up the AACVD $Bi_2WO_6$ film grow more in directions that are favorable to electron transport in comparison to the crystallographic standard (47 vs 36%), at the expense of mixed favorability planes (31 vs 56%). However, a significant and increased fraction of unfavorable growth is also observed (21 vs 9.2%). The predominance of low and mixed growth directions, combined with the presumably random orientation of the crystallites with respect to one another, may account for the extremely slow electron transport observed within the films.

## CONCLUSIONS

In summary, $Bi_2WO_6$ photoanodes were synthesized by AACVD. The coatings possessed rough topography formed of micron-sized mounds made up of smaller crystallites. Our photoanodes showed relatively early onset potentials for photoelectrochemical water oxidation, but low photocurrents in comparison to other better-studied metal oxides. With the exception of $TiO_2$, the ultrafast recombination in $Bi_2WO_6$ was slightly slower than in other oxides, while water oxidation rate constants were similar to those of other metal oxides (except for $WO_3$). However, electron extraction in $Bi_2WO_6$ is 10−100 times slower than in these materials. Analysis of the band structure of $Bi_2WO_6$ obtained from DFT shows that the layered structure of $Bi_2WO_6$ leads to confinement of the CB to the $(WO_4^{2-})_n$ planes running through the material. This localization produces slow electron transport in the direction perpendicular to the CB plane. This concept leads to a clear design principle for $Bi_2WO_6$, as strong preferred or epitaxial growth along the conduction band planes should lead to improved performance. Anisotropic electron transport should, in principle, arise in any layered metal oxide in which the metals are segregated into separate 2d planes, and these results are likely to be of great significance to a wide range of upcoming oxide materials for numerous catalytic processes. We therefore suggest preferred or epitaxial growth along CB planes as a general strategy to overcome poor electron transport in such layered oxides.

## ASSOCIATED CONTENT

### Supporting Information

The Supporting Information is available free of charge at https://pubs.acs.org/doi/10.1021/acs.jpcc.0c03539.

Measured and modeled XRD patterns of AACVD $Bi_2WO_6$ films, XPS spectra of pristine $Bi_2WO_6$, SEM/EDX of a $Bi_2WO_6$ film, diffuse reflectance spectrum, PEC stability under intense UV irradiation, ultrafast TA kinetics, fitting of TA kinetics, analysis of crystal growth planes, literature summary of key properties of $Bi_2WO_6$, and comparison of transient recombination times (PDF).

## AUTHOR INFORMATION


### Corresponding Authors

**Benjamin Moss** − *Department of Chemistry, Molecular Science Research Hub, Imperial College London, London W12 0BZ, U.K.;* orcid.org/0000-0002-5786-1587; Email: b.moss14@imperial.ac.uk

**Andreas Kafizas** − *Department of Chemistry, Molecular Science Research Hub and Grantham Institute for Climate Change, Imperial College London, London W12 0BZ, U.K.;* orcid.org/0000-0002-2282-4639; Email: a.kafizas@imperial.ac.uk

### Authors

**Haonan Le** − *Department of Chemistry, Molecular Science Research Hub, Imperial College London, London W12 0BZ, U.K.*

**Sacha Corby** − *Department of Chemistry, Molecular Science Research Hub, Imperial College London, London W12 0BZ, U.K.;* orcid.org/0000-0001-7863-5426

**Kazuki Morita** − *Department of Materials, Imperial College London, London SW7 2AZ, U.K.;* orcid.org/0000-0002-2558-6963

**Shababa Selim** − *Department of Chemistry, Molecular Science Research Hub, Imperial College London, London W12 0BZ, U.K.;* orcid.org/0000-0001-5398-0661

**Carlos Sotelo-Vazquez** − *Department of Chemistry, University College London, London WC1H 0AJ, U.K.;* orcid.org/0000-0003-0949-4548

**Yunuo Chen** − *Department of Chemistry, Molecular Science Research Hub, Imperial College London, London W12 0BZ, U.K.*

**Alexander Borthwick** − *Department of Chemistry, Molecular Science Research Hub, Imperial College London, London W12 0BZ, U.K.*

**Anna Wilson** − *Department of Chemistry, Molecular Science Research Hub, Imperial College London, London W12 0BZ, U.K.*

**Chris Blackman** − *Department of Chemistry, University College London, London WC1H 0AJ, U.K.;* orcid.org/0000-0003-0700-5843

**James R. Durrant** − *Department of Chemistry, Molecular Science Research Hub, Imperial College London, London W12 0BZ, U.K.;* orcid.org/0000-0001-8353-7345

**Aron Walsh** − *Department of Materials, Imperial College London, London SW7 2AZ, U.K.; Department of Materials Science and Engineering, Yonsei University, Seoul 03722, South Korea;* orcid.org/0000-0001-5460-7033

Complete contact information is available at: https://pubs.acs.org/10.1021/acs.jpcc.0c03539


### Author Contributions

B.M. wrote the research article and carried out PEC, SEM, EDX, and XPS measurements. C.S.-V. carried out HR-TEM measurements. H.L. and Y.C. synthesized the $Bi_2WO_6$ photoanodes, carried out physical characterizations, and measured their photoelectrochemical performance. A.B. carried out photoelectrochemical measurements and conducted a literature review on $Bi_2WO_6$ photoanodes and photocatalysts. S.C. conducted ultrafast TAS studies. K.M. performed DFT calculations. S.S. provided ultrafast TAS data for comparison. A.W. conducted photoelectrochemical measurements. C.B. oversaw and provided access to CVD facilities to carry out this work. J.R.D. oversaw and provided access to TAS facilities. A.W. oversaw and provided access to DFT facilities. A.K. directed the research, helped to draft the manuscript, and carried out slow-timescale TAS measure-



https://dx.doi.org/10.1021/acs.jpcc.0c03539
J. Phys. Chem. C 2020, 124, 18859−18867

ments. All authors contributed to the analysis and editing of the manuscript.

### Notes

The authors declare no competing financial interest.

## ■ ACKNOWLEDGMENTS

B.M. thanks the EPSRC for a doctoral training partnership award. S.C. thanks the Imperial College London for a Schrödinger Scholarship. A.K. thanks the Imperial College for a Junior Research Fellowship, the EPSRC for a Capital Award Emphasising Support for Early Career Researchers, and the Royal Society for an Equipment Grant (RSG\R1\180434). For the CVD equipment used in this work, we thank Mr. Lee Tooley for design and construction and Mr. Steven Atkins for electrical work. We are grateful to the UK Materials and Molecular Modelling Hub for computational resources, which are partially funded by the EPSRC (EP/P020194/1). This research has been partially supported by the Keio University Research Grant for Young Researcher's Program, the Yoshida Scholarship Foundation, the Japan Student Services Organization, and the Centre for Doctoral Training on Theory and Simulation of Materials at Imperial College London.

## ■ REFERENCES

(1) Broecker, W. S. Climatic Change: Are We on the Brink of a Pronounced Global Warming? *Science* **1975**, *189*, 460−463.
(2) Gruber, N. Warming up, Turning Sour, Losing Breath: Ocean Biogeochemistry under Global Change. *Philos. Trans. A. Math. Phys. Eng. Sci.* **2011**, *369*, 1980−1996.
(3) Staffell, I.; Scamman, D.; Abad, A. V.; Balcombe, P.; Dodds, P. E.; Ekins, P.; Shah, N.; Ward, K. R. The Role of Hydrogen and Fuel Cells in the Global Energy System. *Energy Environ. Sci.* **2019**, *12*, 463−491.
(4) Brandon, N. P.; Kurban, Z. Clean Energy and the Hydrogen Economy. *Philos. Trans. R. Soc. A Math. Phys. Eng. Sci.* **2017**, *375*, 20160400.
(5) Sivula, K. Toward Economically Feasible Direct Solar-to-Fuel Energy Conversion. *J. Phys. Chem. Lett.* **2015**, *6*, 975−976.
(6) Shaner, M. R.; Atwater, H. A.; Lewis, N. S.; McFarland, E. W. A Comparative Technoeconomic Analysis of Renewable Hydrogen Production Using Solar Energy. *Energy Environ. Sci.* **2016**, *9*, 2354−2371.
(7) Rothschild, A.; Dotan, H. Beating the Efficiency of Photovoltaics-Powered Electrolysis with Tandem Cell Photoelectrolysis. *ACS Energy Lett.* **2017**, *2*, 45−51.
(8) Yang, Y.; Niu, S.; Han, D.; Liu, T.; Wang, G.; Li, Y. Progress in Developing Metal Oxide Nanomaterials for Photoelectrochemical Water Splitting. *Adv. Energy Mater.* **2017**, *7*, 1700555.
(9) Sivula, K.; Van De Krol, R. Semiconducting Materials for Photoelectrochemical Energy Conversion. *Nat. Rev. Mater.* **2016**, *1*, 15010.
(10) Lee, D. K.; Lee, D.; Lumley, M. A.; Choi, K. S. Progress on Ternary Oxide-Based Photoanodes for Use in Photoelectrochemical Cells for Solar Water Splitting. *Chem Soc Rev. Royal Soc Chem* **2019**, *48*, 2126−2157.
(11) Zhang, N.; Ciriminna, R.; Pagliaro, M.; Xu, Y. J. Nanochemistry-Derived Bi2WO6 Nanostructures: Towards Production of Sustainable Chemicals and Fuels Induced by Visible Light. *Chem. Soc. Rev.* **2014**, *43*, 5276−5287.
(12) Kendall, K. R.; Navas, C.; Thomas, J. K.; Zur Loye, H. C. Recent Developments in Oxide Ion Conductors: Aurivillius Phases. *Chem. Mater.* **1996**, *8*, 642−649.
(13) Morita, K.; Park, J. S.; Kim, S.; Yasuoka, K.; Walsh, A. Crystal Engineering of Bi2WO6 to Polar Aurivillius-Phase Oxyhalides. *J. Phys. Chem. C* **2019**, *123*, 29155−29161.
(14) Kunioku, H.; Higashi, M.; Tomita, O.; Yabuuchi, M.; Kato, D.; Fujito, H.; Kageyama, H.; Abe, R. Strong Hybridization between Bi-6s and O-2p Orbitals in Sillén-Aurivillius Perovskite Bi4MO8X (M = Nb, Ta; X = Cl, Br), Visible Light Photocatalysts Enabling Stable Water Oxidation. *J. Mater. Chem. A* **2018**, *6*, 3100−3107.
(15) Jiang, B.; Zhang, P.; Zhang, Y.; Wu, L.; Li, H.; Zhang, D.; Li, G. Self-Assembled 3D Architectures of Bi 2TiO 4F 2 as a New Durable Visible-Light Photocatalyst. *Nanoscale* **2012**, *4*, 455−460.
(16) Sun, S.; Wang, W.; Jiang, D.; Zhang, L.; Li, X.; Zheng, Y.; An, Q. Bi2WO6 Quantum Dot-Intercalated Ultrathin Montmorillonite Nanostructure and Its Enhanced Photocatalytic Performance. *Nano Res.* **2014**, *7*, 1497−1506.
(17) Zhang, L.; Zhu, Y. A Review of Controllable Synthesis and Enhancement of Performances of Bismuth Tungstate Visible-Light-Driven Photocatalysts. *Catal. Sci. Technol.* **2012**, *2*, 694−706.
(18) Huang, H.; Liu, K.; Chen, K.; Zhang, Y.; Zhang, Y.; Wang, S. Ce and F Comodification on the Crystal Structure and Enhanced Photocatalytic Activity of Bi $_2$ WO $_6$ Photocatalyst under Visible Light Irradiation. *J. Phys. Chem. C* **2014**, *118*, 14379−14387.
(19) Chae, S. Y.; Lee, E. S.; Jung, H.; Hwang, Y. J.; Joo, O. S. Synthesis of Bi2WO6 Photoanode on Transparent Conducting Oxide Substrate with Low Onset Potential for Solar Water Splitting. *RSC Adv.* **2014**, *4*, 24032−24037.
(20) Jian, J.; Jiang, G.; van de Krol, R.; Wei, B.; Wang, H. Recent Advances in Rational Engineering of Multinary Semiconductors for Photoelectrochemical Hydrogen Generation. *Nano Energy* **2018**, *51*, 457−480.
(21) Kudo, A.; Hijii, S. H2 or O2 Evolution from Aqueous Solutions on Layered Oxide Photocatalysts Consisting of Bi3+ with 6s2 Configuration and D0 Transition Metal Ions. *Chem. Lett.* **1999**, *28*, 1103−1104.
(22) Dumrongrojthanath, P.; Thongtem, T.; Phuruangrat, A.; Thongtem, S. Synthesis and Characterization of Hierarchical Multilayered Flower-like Assemblies of Ag Doped Bi2WO6 and Their Photocatalytic Activities. *Superlattices Microstruct.* **2013**, *64*, 196−203.
(23) Zhang, L.; Bahnemann, D. Synthesis of Nanovoid Bi2WO6 2D Ordered Arrays as Photoanodes for Photoelectrochemical Water Splitting. *ChemSusChem* **2013**, *6*, 283−290.
(24) Zhang, L.; Baumanis, C.; Robben, L.; Kandiel, T.; Bahnemann, D. Bi 2WO 6 Inverse Opals: Facile Fabrication and Efficient Visible-Light-Driven Photocatalytic and Photoelectrochemical Water-Splitting Activity. *Small* **2011**, *7*, 2714−2720.
(25) Hill, J. C.; Choi, K. S. Synthesis and Characterization of High Surface Area CuWO4 and Bi2WO6 Electrodes for Use as Photoanodes for Solar Water Oxidation. *J. Mater. Chem. A* **2013**, *1*, 5006−5014.
(26) Dong, G.; Zhang, Y.; Bi, Y. The Synergistic Effect of Bi 2 WO 6 Nanoplates and Co 3 O 4 Cocatalysts for Enhanced Photoelectrochemical Properties. *J. Mater. Chem. A* **2017**, *5*, 20594−20597.
(27) Dong, G.; Zhang, Y.; Wang, W.; Wang, L.; Bi, Y. Facile Fabrication of Nanoporous Bi 2 WO 6 Photoanodes for Efficient Solar Water Splitting. *Energy Technol.* **2017**, *5*, 1912−1918.
(28) Dong, G.; Hu, H.; Wang, L.; Zhang, Y.; Bi, Y. Remarkable Enhancement on Photoelectrochemical Water Splitting Derived from Well-Crystallized Bi 2 WO 6 and Co(OH) x with Tunable Oxidation State. *J. Catal.* **2018**, *366*, 258−265.
(29) Song, X. C.; Zheng, Y. F.; Ma, R.; Zhang, Y. Y.; Yin, H. Y. Photocatalytic Activities of Mo-Doped Bi 2WO 6 Three-Dimensional Hierarchical Microspheres. *J. Hazard. Mater.* **2011**, *192*, 186−191.
(30) Li, Y.; Liu, J.; Huang, X.; Yu, J. Carbon-Modified Bi2WO6 Nanostructures with Improved Photocatalytic Activity under Visible Light. *Dalt. Trans.* **2010**, *39*, 3420−3425.
(31) Fu, Y.; Chang, C.; Chen, P.; Chu, X.; Zhu, L. Enhanced Photocatalytic Performance of Boron Doped Bi2WO6 Nanosheets under Simulated Solar Light Irradiation. *J. Hazard. Mater.* **2013**, *254*−*255*, 185−192.


https://dx.doi.org/10.1021/acs.jpcc.0c03539
J. Phys. Chem. C 2020, 124, 18859−18867

(32) Zhong, Y.; He, Z.; Chen, D.; Hao, D.; Hao, W. Enhancement of Photocatalytic Activity of Bi 2 MoO 6 by Fluorine Substitution. *Appl. Surf. Sci.* **2019**, *467−468*, 740−748.
(33) Zhang, Z.; Wang, W.; Gao, E.; Shang, M.; Xu, J. Enhanced Photocatalytic Activity of Bi 2WO 6 with Oxygen Vacancies by Zirconium Doping. *J. Hazard. Mater.* **2011**, *196*, 255−262.
(34) Hu, J.; Chen, D.; Mo, Z.; Li, N.; Xu, Q.; Li, H.; He, J.; Xu, H.; Lu, J. Z-Scheme 2D/2D Heterojunction of Black Phosphorus/ Monolayer Bi 2 WO 6 Nanosheets with Enhanced Photocatalytic Activities. *Angew. Chem., Int. Ed.* **2019**, *58*, 2073−2077.
(35) Zhao, J.; Yang, Y.; Dong, X.; Ma, Q.; Yu, W.; Wang, J.; Liu, G. Electrospinning Construction of Bi2WO6/RGO Composite Nanofibers with Significantly Enhanced Photocatalytic Water Splitting Activity. *RSC Adv.* **2016**, *6*, 64741−64748.
(36) Rauf, A.; Ma, M.; Kim, S.; Shah, M. S. A. S.; Chung, C. H.; Park, J. H.; Yoo, P. J. Mediator- and Co-Catalyst-Free Direct Z-Scheme Composites of Bi2WO6-Cu3P for Solar-Water Splitting. *Nanoscale* **2018**, *10*, 3026−3036.
(37) Joshi, B.; Yoon, H.; Kim, H.; Kim, M. W.; Mali, M. G.; Al-Deyab, S. S.; Yoon, S. S. Heterojunction Photoanodes for Solar Water Splitting Using Chemical-Bath-Deposited In2O3 Micro-Cubes and Electro-Sprayed Bi2WO6 Textured Nanopillars. *RSC Adv.* **2015**, *5*, 85323−85328.
(38) Hao, H.; Lu, D.; Wang, Q. Photoelectrochemical Study on Charge Separation Mechanisms of Bi2WO6 Quantum Dots Decorated G-C3N4. *Int. J. Hydrogen Energy* **2018**, *43*, 8824−8834.
(39) Godin, R.; Kafizas, A.; Durrant, J. R. Electron Transfer Dynamics in Fuel Producing Photosystems. *Curr. Opin. Electrochem.* **2017**, *2*, 136−143.
(40) Zhang, G.; Hu, Z.; Sun, M.; Liu, Y.; Liu, L.; Liu, H.; Huang, C. P.; Qu, J.; Li, J. Formation of Bi2WO6 Bipyramids with Vacancy Pairs for Enhanced Solar-Driven Photoactivity. *Adv. Funct. Mater.* **2015**, *25*, 3726−3734.
(41) Saison, T.; Gras, P.; Chemin, N.; Chanéac, C.; Durupthy, O.; Brezová, V.; Colbeau-Justin, C.; Jolivet, J. P. New Insights into Bi2WO6 Properties as a Visible-Light Photocatalyst. *J. Phys. Chem. C* **2013**, *117*, 22656−22666.
(42) Zhang, G.; Cao, J.; Huang, G.; Li, J.; Li, D.; Yao, W.; Zeng, T. Facile Fabrication of Well-Polarized Bi 2 WO 6 Nanosheets with Enhanced Visible-Light Photocatalytic Activity. *Catal. Sci. Technol.* **2018**, *8*, 6420−6428.
(43) Zhou, Y.; Zhang, X.; Zhang, Q.; Dong, F.; Wang, F.; Xiong, Z. Role of Graphene on the Band Structure and Interfacial Interaction of Bi2WO6/Graphene Composites with Enhanced Photocatalytic Oxidation of NO. *J. Mater. Chem. A* **2014**, *2*, 16623−16631.
(44) Xie, T.; Liu, Y.; Wang, H.; Wu, Z. Synthesis of $\alpha$-Fe 2 O 3 /Bi 2 WO 6 Layered Heterojunctions by in Situ Growth Strategy with Enhanced Visible-Light Photocatalytic Activity. *Sci. Rep.* **2019**, *9*, 7551.
(45) Corby, S.; Francàs, L.; Selim, S.; Sachs, M.; Blackman, C.; Kafizas, A.; Durrant, J. R. Water Oxidation and Electron Extraction Kinetics in Nanostructured Tungsten Trioxide Photoanodes. *J. Am. Chem. Soc.* **2018**, *140*, 16168−16177.
(46) Physical Sciences Data science Service. https://icsd.psds.ac.uk/
(47) RRUFF database of Raman spectroscopy, X-ray diffraction and chemistry of minerals. https://rruff.info/
(48) Casa Software Ltd. http://www.casaxps.com/
(49) Blöchl, P. E. Projector Augmented-Wave Method. *Phys. Rev. B* **1994**, *50*, 17953−17979.
(50) Kresse, G.; Furthmüller, J. Efficient Iterative Schemes for Ab Initio Total-Energy Calculations Using a Plane-Wave Basis Set. *Phys. Rev. B - Condens. Matter Mater. Phys.* **1996**, *54*, 11169−11186.
(51) Kresse, G.; Furthmüller, J. Efficiency of Ab-Initio Total Energy Calculations for Metals and Semiconductors Using a Plane-Wave Basis Set. *Comput. Mater. Sci.* **1996**, *6*, 15−50.
(52) Momma, K.; Izumi, F. VESTA 3 for Three-Dimensional Visualization of Crystal, Volumetric and Morphology Data. *J. Appl. Crystallogr.* **2011**, *44*, 1272−1276.
(53) Kafizas, A.; Francàs, L.; Sotelo-Vazquez, C.; Ling, M.; Li, Y.; Glover, E.; McCafferty, L.; Blackman, C. S.; Darr, J. A.; Parkin, I. P. Optimizing The Activity of Nano-Needle Structured WO3 Photoanodes for Solar Water Splitting − Direct Synthesis Via Chemical Vapor Deposition. *J. Phys. Chem. C* **2017**, *121*, 5983−5993.
(54) Rae, A. D.; Thompson, J. G.; Withers, R. L. Structure Refinement of Commensurately Modulated Bismuth Tungstate, Bi2WO6. *Acta Crystallogr. Sect. B Struct. Sci.* **1991**, *47*, 870−881.
(55) Yashima, M.; Ishimura, D. Crystal Structure and Disorder of the Fast Oxide-Ion Conductor Cubic Bi2O3. *Chem. Phys. Lett.* **2003**, *378*, 395−399.
(56) Pendlebury, S. R.; Wang, X.; Le Formal, F.; Cornuz, M.; Kafizas, A.; Tilley, S. D.; Grätzel, M.; Durrant, J. R. Ultrafast Charge Carrier Recombination and Trapping in Hematite Photoanodes under Applied Bias. *J. Am. Chem. Soc.* **2014**, *136*, 9854−9857.
(57) Moss, B.; Lim, K. K.; Beltram, A.; Moniz, S.; Tang, J.; Fornasiero, P.; Barnes, P.; Durrant, J.; Kafizas, A. Comparing Photoelectrochemical Water Oxidation, Recombination Kinetics and Charge Trapping in the Three Polymorphs of $TiO_2$. *Sci. Rep.* **2017**, *7*, 2938.
(58) Sachs, M.; Pastor, E.; Kafizas, A.; Durrant, J. R. Evaluation of Surface State Mediated Charge Recombination in Anatase and Rutile TiO2. *J. Phys. Chem. Lett.* **2016**, *7*, 3742−3746.
(59) Selim, S.; Pastor, E.; García-Tecedor, M.; Morris, M. R.; Franca, L.; Sachs, M.; Moss, B.; Corby, S.; Mesa, C. A.; Gimenez, S.; Kafizas, A.; Bakulin, A. A.; Durrant, J. R. Impact of Oxygen Vacancy Occupancy on Charge Carrier Dynamics in BiVO 4 Photoanodes. *J. Am. Chem. Soc.* **2019**, *16*, 12.
(60) Nelson, J.; Chandler, R. E. Random Walk Models of Charge Transfer and Transport in Dye Sensitized Systems. *Coord. Chem. Rev.* **2004**, *248*, 1181−1194.
(61) Ma, Y.; Pendlebury, S. R.; Reynal, A.; Le Formal, F.; Durrant, J. R. Dynamics of Photogenerated Holes in Undoped BiVO4 Photoanodes for Solar Water Oxidation. *Chem. Sci.* **2014**, *5*, 2964.
(62) Zachäus, C.; Abdi, F. F.; Peter, L. M.; Van De Krol, R. Photocurrent of BiVO4 Is Limited by Surface Recombination, Not Surface Catalysis. *Chem. Sci.* **2017**, *8*, 3712−3719.
(63) Kafizas, A.; Ma, Y.; Pastor, E.; Pendlebury, S. R.; Mesa, C.; Francas, L.; Le Formal, F.; Noor, N.; Ling, M.; Sotelo-Vazquez, C.; Carmalt, C. J.; Parkin, I. P.; Durrant, J. R. Water Oxidation Kinetics of Accumulated Holes on the Surface of a TiO2 Photoanode: A Rate Law Analysis. *ACS Catal.* **2017**, *7*, 4896−4903.
(64) Le Formal, F.; Pendlebury, S. R.; Cornuz, M.; Tilley, S. D.; Graetzel, M.; Durrant, J. R. Back Electron − Hole Recombination in Hematite Photoanodes for Water Splitting. *J. Am. Chem. Soc.* **2014**, *136*, 2564−2574.
(65) Walsh, A.; Yan, Y.; Huda, M. N.; Al-Jassim, M. M.; Wei, S. H. Band Edge Electronic Structure of BiVO 4: Elucidating the Role of the Bi s and V d Orbitals. *Chem. Mater.* **2009**, *21*, 547−551.


https://dx.doi.org/10.1021/acs.jpcc.0c03539
J. Phys. Chem. C 2020, 124, 18859−18867